https://doi.org/10.5194/essd-2022-27
Preprint. Discussion started: 8 February 2022

Open Access Earth System Science Data Discussions

The FY-3D Global Active Fire product: Principle, Methodology and Validation

Jie Chen[1]†, Qi Yao[2]†, Ziyue Chen[2]*, Manchun Li[3], Zhaozhan Hao[4], Cheng Liu[1], Wei Zheng[1], Miaoqing Xu[2], Xiao Chen[2], Jing Yang[2], Qiancheng Lv[2], Bingbo Gao[4]*

[1] National Satellite Meteorological Center, China Meteorological Administration, Beijing 100081, China

[2] College of Global Change and Earth System Science, Beijing Normal University, Beijing 100091, China

[3] School of Geography and Ocean Sciences, Nanjing University, Nanjing 210008, China

[4] College of Land Science and Technology, China Agricultural University, Beijing 100083, China

†These authors contributed equally.

**Correspondence to*: Ziyue Chen (zychen@bnu.edu.cn) or Bingbo Gao (gaobingbo@cau.edu.cn)

Abstract. Wild fires have a strong negative effect on environment, ecology and public health. However, the continuous degradation of mainstream global fire products leads to large uncertainty on the effective monitoring of wild fires and its influence. To fill this gap, we produced FY-3D global fire products with a similar spatial and temporal resolution, aiming to serve as the continuity and replacement for MODIS fire products. Firstly, the sensor parameters and major algorithms for noise detection and fire identification in FY-3D products were introduced. For accuracy assessment, five typical regions, Africa, South America, Indo-China Peninsula， Siberia and Australia, across the globe were selected. The overall consistence between FY-3D fire products and reference data exceeded 94%, with a more than 90% consistence in all regions. Furthermore, the consistence between FY-3D and MODIS fire products was examined. The result suggested that the overall consistence was 84.4%, with a fluctuation across seasons, surface types and regions. The high accuracy and consistence with MODIS products proved that FY-3D fire product was an ideal tool for global fire monitoring. Specially, since detailed geographical conditions in China were considered, FY-3D products should be preferably employed for fires monitoring in China. FY-3D fire dataset can be downloaded at http://satellite.nsmc.org.cn/portalsite/default.aspx (NSMC, 2021).

1 Introduction

More than half of global land surfaces have been influenced by wild fires and the total global burned area summed up to the area of European Union every year (Andela et al., 2019; Keeley et al., 2011; Moritz et al., 2012). Wild fires, especially large-scale wild fires, in forests, grasslands and farmlands have a significant impact on crop productivity (Jethva et al., 2019), atmospheric pollution (Guo et al., 2020), biodiversity (Kelly et al., 2020), climate change (Alisjahbana et al., 2017; Keegan et al., 2014) and public health (Huff et al., 2015; Johnston et al., 2012; Oliveira et al., 2020; Yuchi et al., 2016). In recent years, the increasing events of forest fires in China, US, Australia, and Amazon Rain Forests and grassland fires in Mongolia have caused a large number of casualty (Cochrane, 2003), millions of lost wildlife (Wintle et al., 2020), remarkably deteriorated air quality (Liu et al., 2018; Marlier et al., 2012; Volkova et al.,

https://doi.org/10.5194/essd-2022-27
Preprint. Discussion started: 8 February 2022

2019), severely damaged ecosystems (Cerda et al., 2012), massive economic losses (Stephenson et al., 2013) and regional or global climate change (Abram et al., 2021; Jacobson, 2014).

Due to its great influences, growing emphasis has been placed on the monitoring of wild fires based on remote sensing products. Since 1970s, the implementation and research of satellite-based fire detection has started in US using National Oceanic and Atmospheric Administration (NOAA) series satellites (www.noaa.gov, Dozier et al., 1981; Flannigan and Haar et al., 1986; Kaufman et al., 1990; Boles et al., 2000). NOAA fire products, with a spatial resolution of 1.1 km and a daily temporal resolution, have been employed globally for decades, and provide the data support for long time series analysis. In addition to NOAA fire products, a diversity of regional or global fire products has been proposed in recent years.

Thanks to its easy access, long time series, and reliable accuracy (Giglio et al., 2003), the Moderate Resolution Imaging Spectroradiometer (MODIS) fire product, with a spatial resolution of 1km and a temporal resolution of 12 hours, have been available since 2000 and become one of the most widely employed fire products to monitor the temporal evolution of large-scale wide fires, including forest fires (Mohajane et al., 2021), grassland fires (Zhang et al., 2017) and crop residue burning (Li et al., 2016). With a similar temporal resolution (12 hours), the Visible Infrared Imaging Radiometer Suite (VIIRS) fire products with a spatial resolution of 375m has been available for fire detection since 2011. Despite a higher spatial resolution, VIIRS fire products are produced using less bands than MODIS fire products, and the mainly used 4-µm I-band may lead to large bias in the estimation of FRP (Fire Radiative Power) during an intense fire event (Schroeder et al., 2014). Consequently, VIIRS fire products present a relatively poor consistence with MODIS fire products and the accuracy of VIIRS fire products is generally lower than that of MODIS fire products (Sharma et al., 2017). In this case, VIIRS fire products may not serve as a complete replacement of and should be comprehensively employed with MODIS fire products. Available since 2013, Landsat fire products employ the visible and near infrared (VNIR) and short-wave infrared (SWIR) bands of the Landsat-8 imagery to detect thermal anomalies (Kumar and Roy, 2017; Murphy et al., 2016; Schroeder et al., 2016). Its spatial and temporal resolution is 30 m and 16 days, respectively. Despite its fine spatial resolution, its coarse temporal resolution makes this data source not suitable for monitoring the occurrence and evolution of wild fires. Instead, Landsat fire products are more frequently employed for identifying the post-fire areas.

In recent years, with the growing needs for real-time monitoring of a diversity of environmental issues and ecological process, some satellites have been launched to provide remote sensing products with extremely high temporal resolution. GEOS-16 Advanced Baseline Imager (ABI) active fire products, with a temporal resolution of five minutes and a spatial resolution of 2km, have been available since 2017. GEOS-ABI fire products can effectively monitor middle to large-scale fires and be used for estimating fire emissions. GEOS-ABI fire products may lead to a poor detection accuracy when identifying small-scale fires (Li et al., 2020). GEOS-ABI mainly provides regional fire products in Southeastern Conterminous United States (CONUS). Himawari-8 products, with a spatial resolution of 2 km and temporal resolution of 10 minutes, have been widely employed to monitor meteorology and

https://doi.org/10.5194/essd-2022-27
Preprint. Discussion started: 8 February 2022

wild fires in Asia and Australia since 2015 (Xu et al. 2017). Similar to GEOS-16 ABI fire products, Himawari-8 fire products are also limited in effectively detecting small-scale fires (Wickramasinghe et al., 2018). Despite an extremely high temporal resolution, fire products produced using geostationary satellites only cover a regional area and cannot monitor the distribution and evolution of wild fires at a global scale.

With the ageing of existing mainstream global fire monitors (e.g. MODIS), their accuracy and reliability presented a notable decrease (Wang et al., 2012) and can no longer provide high-quality data for effective fire monitoring and a series of relevant studies. Therefore, there is a growing need for alternative global fire products. Since the launch of Fengyun-3C (FY-3C) satellite in September, 2013, a series of FY meteorological satellites have been designed to produce global active fire products. FY-3C VIRR fire products were produced based on an effective active fire detection algorithm (Lin et al., 2017), which considered dynamic thresholds and infrared gradients. However, the overall accuracy of FY-3C VIRR fire products remained unsatisfactory at the global scale and are thus not publicly released.

In November, 2017, Fengyun-3D (FY-3D) satellite was launched with an improved Medium Resolution Spectral Imager (MERSI) for fire detection, which provides a promising solution for replacing existing fire products. In this paper, we introduce the characteristics and fire detection algorithms of a new global fire products based on FY-3D (recently downloadable from our official website http://satellite.nsmc.org.cn/portalsite/default.aspx). Furthermore, this fire product is comprehensively compared with other mainstream fire products, especially MODIS global fire products. The new FY-3D global fire products aim to serve as a continuity of existing, yet degrading MODIS fire products and better support regional (especially Asia) and global ecological and environment research.

2 The overview of FY-3 fire products

2.1 Instrument

As one of the core instruments of the Fengyun-3 (FY-3) satellite, the updated medium resolution spectral imager (MERSI) can be comparable with the imaging instrument of the latest polar-orbiting meteorological satellite launched by the United States, and has become one of the most advanced remote sensing instruments based on wide swath imaging. FY-3D satellite was launched in November 2017 with 10 sets of remote sensing instruments, including the medium resolution spectral imager (MERSI-II), microwave temperature sounder (MWTS-II), microwave humidity sounder (MWHS-II), hyper-spectral infrared atmospheric sounder (HIRAS), microwave radiation imager (MWRI), near-infrared hyper-spectral greenhouse gas monitor (GAS), wide-angle aurora imager (WAI-I), iono-spheric photometer (IPM), space environment monitor (SEM), and global navigation occultation sounder (GNOS) (National Satellite Meteorological Center, 2010).

MERSI-II integrates the functions of the original two imaging instruments (MERSI-I and VIRR) of FY-3B and FY-3C, with a total of 25 channels, including visible light, near infrared, medium infrared, and

https://doi.org/10.5194/essd-2022-27
Preprint. Discussion started: 8 February 2022

far infrared (As Table 1). The infrared imaging, detection sensitivity, and calibration accuracy of MERSI-II are improved greatly. It is the first imaging instrument that can access the 250-meter resolution infrared split-window area globally and capture seamless 250-meter resolution true color global images on a daily basis. MERSI-II also enables the high-quality retrieval of atmospheric, land, and marine parameters such as clouds, aerosols, vapor, land surface features, and ocean color, supporting global support for environment and climate issues.

Table 1 FY-3D/MERSI-II channel parameters

Channel	Wavelength/μm	Waveband	Resolution/km
1	0.470	Visible light	0.25
2	0.550	Visible light	0.25
3	0.650	Visible light	0.25
4	0.865	Near infrared	0.25
5	1.24/1.03	Near infrared	1.00
6	1.640	Near infrared	1.00
7	2.130	Near infrared	1.00
8	0.412	Visible light	1.00
9	0.443	Visible light	1.00
10	0.490	Visible light	1.00
11	0.555	Visible light	1.00
12	0.670	Visible light	1.00
13	0.709	Visible light	1.00
14	0.746	Visible light	1.00
15	0.865	Near infrared	1.00
16	0.905	Near infrared	1.00
17	0.936	Near infrared	1.00
18	0.940	Near infrared	1.00
19	1.380	Near infrared	1.00
20	3.800	Medium infrared	1.00
21	4.050	Medium infrared	1.00
22	7.200	Far infrared	1.00
23	8.550	Far infrared	1.00
24	10.800	Far infrared	0.25
25	12.000	Far infrared	0.25

2.2 Product overview

The global fire monitoring by FY-3D satellite is mainly based on the sensitivity of MERSI-II Channel 20 (mid-infrared channel) to high-temperature heat sources (fire spots). According to the calculation, the emissivity of forest and grassland fires in the mid-infrared band can be hundreds of times higher than that of the surface at normal temperature, making the radiance and brightness temperature of the fire-spot significantly higher than surrounding pixels. For rapid monitoring of global wildfires, it is necessary

https://doi.org/10.5194/essd-2022-27
Preprint. Discussion started: 8 February 2022

Open Access Earth System Science Data Discussions

to develop an algorithm for the automatic identification of fire spots.

MERSI-II fire monitoring products from FY-3D satellite can provide fire spot location, sub-pixel fire spot area, temperature, and fire spot intensity, in inland areas around the world and generate global fire-spot pixel information (including day and night) in an HDF format. FY-3D fire products are produced following a projection with the equal latitude and longitude (0.01°). Fire spot intensity is classified according to sub-pixel fire spot area and temperature, with an overall accuracy above 85%. Based on daily monitoring products, SMART (Satellite Monitoring Analyzing and Remote sensing Tools) system can generate the images of global monthly fire spot distribution, with a resolution of 0.25°.

The algorithm for fire spot identification depends on the sensitivity of mid-infrared channels to high-temperature heat sources. The radiance and brightness temperature of the pixels in the mid-infrared channels with sub-pixel fire spots are higher than those of the surrounding non-fire pixels and those of the pixels in the far-infrared channels. Therefore, the pixels with fire spots can be identified by setting an appropriate threshold, and the estimation of background temperature is the key to high detection accuracy and sensitivity.

Sub-pixel fire spot estimation relies on the brightness temperature in mid-infrared channels, and the far-infrared channels are employed when the mid-infrared channels have saturated brightness temperature. In the single-channel estimation formula, the temperature of the open flame spot is set to 750 K.

Fire spot intensity, namely fire radiation power (FRP), is obtained by substituting the area and temperature of sub-pixel fire spots into the Stephen–Boltzmann formula of full-band blackbody radiation.

$$J^* = \varepsilon\sigma T^4 \ , \tag{1}$$

The radiant emittance J^* has dimensions of energy flux, and the SI units of measure are joules per second per square meter. The SI unit for absolute temperature T is the kelvin. ε is the emissivity for the grey body; if it is a blackbody, $\varepsilon = 1$. σ is the Stephen–Boltzmann constant.

FRP is divided into 10 levels, indicating different ranges of radiation intensity and the fire behavior at fire-spot pixels. Fire spots are classified into four groups with regard to credibility, namely the real fire spots, possible fire spots, fire spots affected by the cloud and noisy(fire spots disturbed by clouds and noise).

FY-3D/MERSI-II daily global fire monitoring products is illustrated in Fig. 1. The major processing of daily fire spot products is the generation of 5-minute fire spot lists, which includes such information as observation time of fire spot pixels, latitude and longitude, sub-pixel fire spot area and temperature, and FRP. Next, all the 5-minute fire spot information for each day is merged into the daily global fire information list.

FY-3D/MERSI-II monthly global fire monitoring products consist of the information list of global fire spot pixels and the density map of global fire spots. The information list of monthly global fire spots

https://doi.org/10.5194/essd-2022-27
Preprint. Discussion started: 8 February 2022

covers all global fire spot pixels in this month. Concerning the multi-time monitoring information of the same pixel, the maximum fire spot area is taken as the current-month fire spot information for the pixel. Fig. 2 is an illustration of the density map of global fire spots based on FY-3D/MERSI-II, in which different colors indicate the number of fire spot pixels at 0.25° × 0.25° spatial grid. Compared with daily FY-3D fire products, monthly FY-3D fire products were advantageous of revealing the global patterns of fire spots. As shown in Fig. 2, the global fire spots were mainly distributed in southern Africa, central South America, southern North America, north-central Asia, and northern Australia in June, 2019.

https://doi.org/10.5194/essd-2022-27
Preprint. Discussion started: 8 February 2022

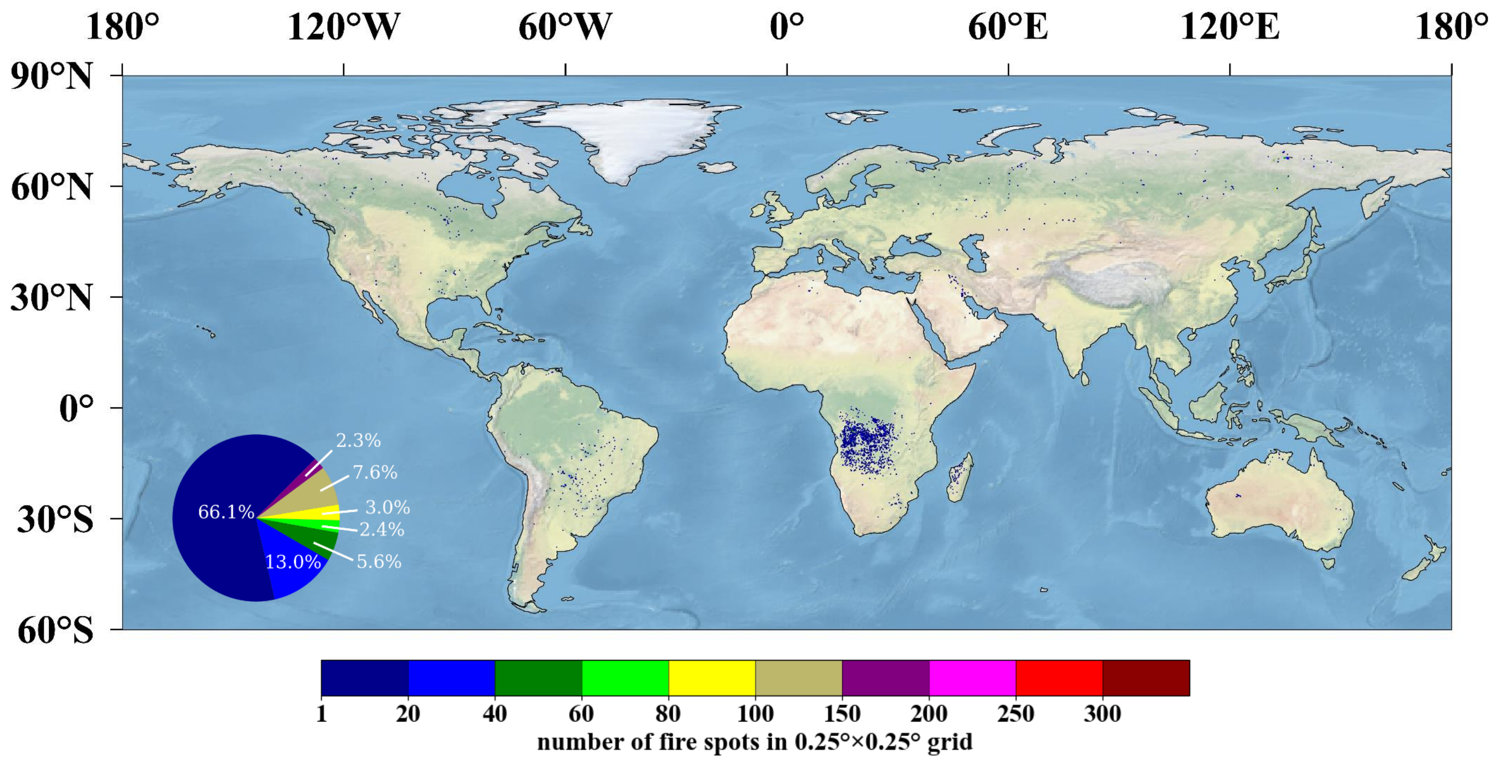

Figure 1 Thematic map of global fire monitoring by FY-3D (2019-06-13). The color bar with different colors means the number of fire spots in the 0.25° × 0.25° grid.

https://doi.org/10.5194/essd-2022-27
Preprint. Discussion started: 8 February 2022

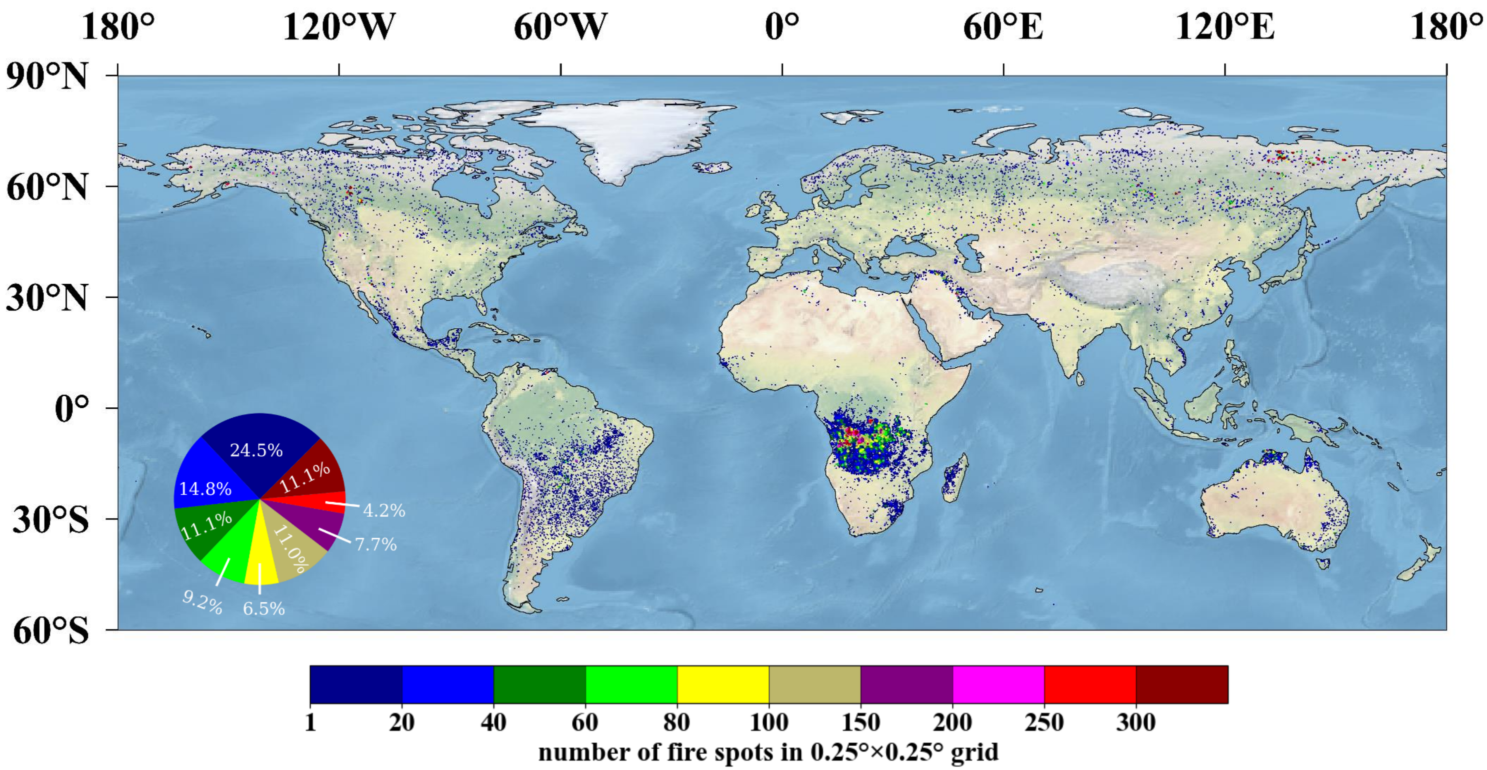

Figure 2 Density map of global fire spots based on FY-3D (2019-06). Fire-prone areas are distributed in northern Russia, south-central Africa, southeastern South America, coastlands of Australia and small parts of Canada.

https://doi.org/10.5194/essd-2022-27
Preprint. Discussion started: 8 February 2022

Open Access Earth System Science Data Discussions

3 Methods

This section mainly introduces the specific algorithm and steps for generating FY-3D global fire products based on the original data obtained from MERSI-II. The input data include MERSI-II global orbital Earth observations, MERSI-II global orbital geographical locations, MERSI-II global orbital cloud detection data, and global land and sea template data, as shown in Table 2.

Table 2 Input file list of MERSI-II global fire monitoring software.

No.	Item	Format	Data type	Period	Source	Description
1	MERSI-II global orbital Earth observations	hdf	1B	Real-time	Preprocessor	Data file after preprocessing 5-minute data segments of MERSI-II
2	MERSI-II global orbital geolocations	hdf	Float	Real-time	Preprocessor	Locations after preprocessing 5-minute data segments of MERSI-II
3	MERSI- II global orbital cloud detection data	hdf	Float	Real-time	Product system	5-minute cloud detection products of MERSI-II produced by the product system
4	Global land and sea template data	dat	Grid	Static	Data management and user service subsystem	Global land-sea boundaries

Automatic identification of fire spots is the major step for generating fire products. Firstly, the 5-minute L1 data segments of MERSI-II and various auxiliary data are read in, and the noise lines are identified to generate the noise line mark. Next, the 5-minute data segments are projected according to rule of the equal latitude and longitude, and cut as 5° × 5° grids to generate a local map.

Secondly, fire spots in each 5° × 5° local map are identified pixel by pixel, subject to the calculation of sub-pixel fire spot area and the estimation of FRP. According to the credibility, the identified fire spot pixels are classified into four categories. Subsequently, all the 5° × 5° local fire spot information in the 5-minute data segments is synthesized to generate fire-spot HDF file products. The general steps for producing FY-3D fire products is briefly explained in Fig 3 and the detailed procedures are explained as follow.

https://doi.org/10.5194/essd-2022-27
Preprint. Discussion started: 8 February 2022

Figure 3 General flow chart of the processing algorithm for FY-3D MERSI-II fire spot products.

3.1 The general principle of fire detection based on MERSI-II

Channel 20 of FY-3D MERSI-II is mid-infrared, with a wavelength of 3.55–3.95 μm, while Channels 24 and 25 are far-infrared, with a wavelength of 10.3–11.3 μm and 11.5–12.5 μm, respectively. According to Wien's displacement law,

$$\lambda * T = b \quad , \tag{2}$$

where λ is the peaks at the wavelength, T is the absolute temperature, b is a constant of proportionality called Wien's displacement constant, equal to about 2898 μm · K. blackbody temperature T is inversely proportional to peak radiation wavelength λ_{max}, as the higher temperature can lead to the smaller peak radiation wavelength. The peak radiation wavelength of the surface at normal temperature (about 300 K)

https://doi.org/10.5194/essd-2022-27
Preprint. Discussion started: 8 February 2022

is close to that of Channels 24 and 25; the combustion temperature of forest fires is generally 500 K–1200 K, and the peak wavelength of thermal radiation is close to that of Channel 20. When a fire spot appears in the observed pixel, the radiance increment in Channel 20 caused by the high temperature in the small sub-region of the pixel, where the fire spot is located (Since the pixel resolution of the scanning radiometer is 1.1 km, it is usually not be all open flame areas at the same time in such a large range), is much higher than surrounding pixels without an open flame and also greater than that in Channels 24 and 25. In this case, the weighted average of radiance increase and brightness temperature increase of each channel differ notably in this pixel, based on which the fire information can be extracted and analyzed.

As indicated by Fig. 4(a), when the fire spot temperature grows, the brightness temperature of CH20 pixels increases rapidly. Even if the fire spot only accounts for 0.1% the pixel area, the brightness temperature increment can reach 10 K (44K) when the fire spot is 500 K (900 K). Although the brightness temperature increase of CH24 also rises with the higher fire spot temperature, it is far lower than that of CH20. Fig. 4(b) illustrates that as the fire spot area gets larger, the brightness temperature of CH20-mixed-pixels grows rapidly. It reaches 12K when the fire spot is 900 K, even if the fire spot only accounts for 0.01% of the pixel area. Similarly, the brightness temperature increment of CH24 grows at a much lower rate than CH20.

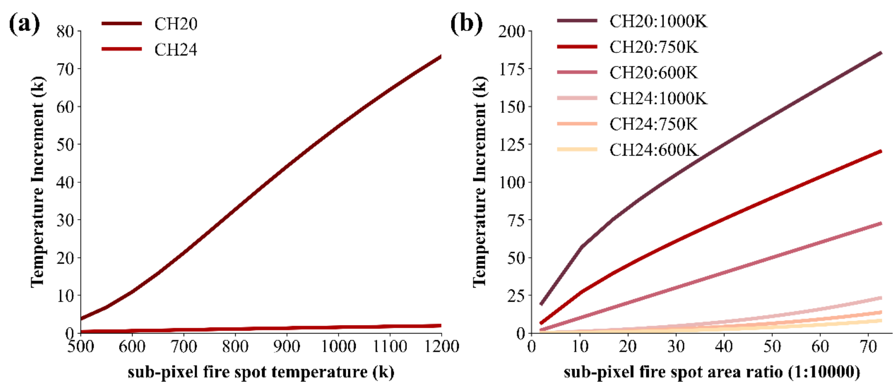

Figure 4 (a): Curves of FY-3D/MERSI-IICH20 and CH24 brightness temperature increment with fire spot temperature (with fire spot area accounting for 0.1% of pixel area and background temperature at 290 K). (b): Curves of FY-3D/MERSI-IICH20 and CH24 brightness temperature increment with fire spot area (with fire spot temperature at 600 K, 750 K, and 1000 K, background temperature at 290 K, and the ratio of fire spot area to pixel area increasing from 0.01% to 0.4%).

3.2 Automatic identification algorithms for fire spots

3.2.1 Detection of cloud pixels

Effective cloud detection is required for generating reliable fire products for the following reasons. Firstly, the existence of cloud in the atmospheric layers may block the emitted information of fire spots, leading to missed identification. Secondly, specular reflection of cloud can lead to wrong identification of fire

https://doi.org/10.5194/essd-2022-27
Preprint. Discussion started: 8 February 2022

spots. Therefore, cloud identification was conducted before fire identification. Similar to MODIS, FY-3D also included radiation information from multiple bands and the principle of cloud identification for FY-3D fire products was similar to that of MODIS. Based on the reflectance difference between cloud and land pixels, we classified cloud pixels following the rules listed in Table 3.

Table 3 major rules for cloud pixel determinations.

number	conditions
1	$T_{Mir} - T_{far1} < 4$K
2	$T_{Mir} - T_{far1} > 20$K & $T_{Mir} < 285$K | $T_{far1} < 280$K
3	$R_{Vis} > 0.28$ & SolarZenith < 70° | SolarZenith <60° & SateZenith < 60°
4	$T_{far1} < 265$K
5	$T_{Mir} < 270$K & $T_{far1} - T_{far2} < 4$K
6	$T_{far1} < 270$K & $T_{far1} - T_{far2} > 60$K
7	$T_{Mir} < 320$K & $T_{Mir} < T_{Mir\_TH}$
8	SolarZenith > 70 & $R_{Vis} > 0.28$ $T_{Mir} < 320$K

T_{Mir}: Mid-infrared channel; T_{far1}: 10.8um Far-infrared channel; T_{far2}: 12um Far-infrared channel; R_{Vis}: Visible light channel; SolarZenith: Solar zenith angle; SateZenith: Satellite zenith angle.

3.2.2 Calculation of background temperature

According to the principle of fire spot identification, when a fire spot appears in a pixel (i.e., open flame), the brightness temperature of the pixel in Channel 20 is significantly higher than the background brightness temperature (the brightness temperature of surrounding non-fire pixels); the brightness temperatures of Channels 24 and 25 are also higher than the background, but the temperature difference is much smaller than Channel 20. In this case, the difference of brightness temperature between fire-spot pixels and background in both the mid-infrared channel and far-infrared channels can be employed as important factors for automatic identification of fire spots. Therefore, the background temperature of the detected pixel is required for identifying fire spots. Since the background temperature cannot be obtained from the fire-spot pixels, it should be calculated according to the average of their surrounding pixels. However, the reflection of solar radiation during the daytime also causes a higher brightness temperature in the mid-infrared channel, which mainly occurs in the zone bare of vegetation, cloud surface, and water bodies (specular reflection). In particular, the difference of brightness temperature between mid-infrared and far-infrared channels caused by specular reflection of solar radiation can reach tens of K on the cloud surface and water bodies. Since the reflection of solar radiation on the bare surface is relatively weak in the mid-infrared channel, a few degrees of difference can cause non-fire pixels misclassified as fire pixels, due to the high sensitivity requirement for fire identification. When the background brightness temperature is calculated, pixels that already contain fire spots should also be excluded. Therefore, suspected high-temperature pixels, which may already contain fire spot pixels, cloudy pixels, water pixels and those pixels affected by solar flare should be removed for background temperature calculation.

Furthermore, the pixel size in the mid-infrared channel of a meteorological satellite is about 1 km^2. Within

https://doi.org/10.5194/essd-2022-27
Preprint. Discussion started: 8 February 2022

Open Access Earth System Science Data Discussions

this range, the underlying surface may be diversified and composed of sub-regions with different fractional vegetation cover (FVC). In the daytime, affected by solar radiation, the brightness temperature of different FVC may vary, making the calculated background temperature higher than expected. To address this issue, Kaufman et al. (1998) suggested the use of standard deviation of background temperature for fire identification, which significantly reduced the overestimation of background temperature caused by different underlying surfaces.

After above-mentioned disturbing pixels were removed, the average and standard deviation of background temperature in the mid-infrared channel, and the background average and standard deviation of brightness temperature difference between the mid-infrared and far-infrared channels were calculated with peripheral pixels as background pixels.

The calculation of background temperature was acquired in the following steps. For each 3×3 window, the background temperature is calculated as the mean temperature of all background pixels. Suspicious high-temperature pixels can be identified according to the following conditions:

$T_{Mir} > T_{th}$ or $T_{Mir} > T'_{Mir\_bg} + \triangle T_{Mir\_bg}$

Where T_{Mir} is the bright temperature in the middle-infrared channel. T_{th} is the threshold for high-temperature pixels in the middle-infrared channel, usually set as sum of the mean bright temperature of all pixels in the window and 2 × its corresponding standard deviation. T'_{Mir_bg} is the mean bright temperature of background pixels.

$\triangle T_{Mir\_bg}$ is the allowed difference between the mean background bright temperature and the suspicious high-temperature pixel, usually set as 2.5 × standard deviation of background pixels. If there were less than 20% of pixels were cloudless pixels, then the 3 ×3 window was extended to 5 ×5, 7×7, 9 × 9…51 × 51. If still not applicable, then this pixel was marked as a non-fire pixel.

3.2.2 Identification of fire pixels

With obtained background temperature, the difference between brightness temperature and background temperature in the mid-infrared channel, as well as the difference of brightness temperature and background temperature between mid-infrared and far-infrared channels, at the candidate pixels could be calculated, based on which we could decide whether the threshold of fire spot identification was reached. If the threshold was reached, the pixel will be preliminarily marked as a fire pixel. Next, for daytime observation data, it is necessary to further check whether the increase of brightness temperature in the mid-infrared channel was interfered by solar radiation in the cloud area. Through the two-stage check, fire pixels could be effectively extracted.

When the following two conditions are met, a pixel can be identified as fire pixel:

(1) $T_{3.9} > T_{3.9bg} + n_1 \times \delta T_{3.9bg}$

(2) $\Delta T_{3.9\_11} > \Delta T_{3.9bg\_11bg} + n_2 \times \delta T_{3.9bg\_11bg}$

Where T_{39} is the bright temperature of the pixel at 3.9 um. $T_{3.9bg}$ is the background bright temperature.

https://doi.org/10.5194/essd-2022-27
Preprint. Discussion started: 8 February 2022

Open Access Earth System Science Data Discussions

$\delta T_{3.9bg}$ is the standard deviation of bright temperature of background pixels. $\Delta T_{3.9\_11}$ is the difference of bright temperature between 3.9 um and 11 um. $\Delta T_{3.9bg\_11bg}$ is the difference of background bright temperature between 3.9 um and 11 um. The setting of this condition aimed to identify the difference of land cover types in the window. When the land cover types in the window were generally consistent, $\delta T_{3.9bg\_11bg}$ is relatively small. For the identification of fire pixels, when $\delta T_{3.9bg\_11bg}$ was smaller than 2k, this value was replaced using 2K. When $\delta T_{3.9bg\_11bg}$ was larger than 4k, this value was replaced using 4K. n_1 and n_2 are background coefficients, which varies across regions, observation time and observation angles. For instance, for Northern grasslands, n_1 and n_2 was set as 3 and 3.5, respectively.

3.2.3 Identification of noise line

Satellite data received by the ground system contain noise. For instance, some scanning lines may contain many noisy pixels that affect fire spot identification. In this case, noise lines, referred to multiple consecutive noisy pixels in one scanning line, should be checked firstly. Since the identification of fire was carried out on the areal map projected with an equal latitude and on the same circle of longitude, the identified latitude and longitude of fire spots failed to reflect the original positions of scanning lines. Therefore, the noise line was identified on the 5-minute data segments before projection. Firstly, the 5-minute data segments were employed to identify fire spots, and the line number of identified fire spot pixels was recorded. Following this, the number of fire spot pixels in each line was counted. When the number of fire spot pixels in a line exceeded the empirical threshold, it was identified as a noise line, and all pixels in the line are marked as noisy ones. In the following process, all pixels in this line were no longer considered for fire-spot identification.

3.3 Estimation of fire radiation power (FRP)

FRP can be calculated using Stephen–Boltzmann formula (Matson et al., 1984) through the estimation of sub-pixel fire spot area and temperature.

3.3.1 Estimation of sub-pixel fire spot area and temperature

MERSI-II data is 12 bits, with a quantization level of 0–4095 and high radiation resolution. The spatial resolution is 1.1 km, and the radiance of a pixel observed by the satellite is the weighted average of the radiance of all the ground objects within the pixel range, as

$$N_t = (\sum_{i=1}^{n} \Delta S_i N_{Ti}) / S \quad , \qquad (3)$$

where N_t is the radiance of the pixel observed by the satellite; t is the brightness temperature corresponding to N_t; $\triangle S_i$ is the area of the i^{th} sub-pixel; N_{Ti} is the radiance of the sub-pixel; Ti is the temperature of the sub-pixel; S is the total area of the pixel.

Due to different FRP and temperature, underlying surfaces containing fire spots can be divided into fire zones and non-fire zones (background). When fire spots appear, the radiance of pixels containing fire spots (i.e. mixed pixels) can be expressed by the following formula:

https://doi.org/10.5194/essd-2022-27
Preprint. Discussion started: 8 February 2022

$$N_{imix} = P * N_{ihi} + (1 - P) * N_{ibg} = P * \frac{C_1 V_i^3}{e^{\frac{C_2 V_i}{T_{hi}}} - 1} + (1 - P) * \frac{C_1 V_i^3}{e^{\frac{C_2 V_i}{T_{bg}}} - 1} , \quad (4)$$

where P is the percentage of sub-pixel fire spot area in the pixel; N_{imix}, N_{ihi}, and N_{ibg} are the radiance of mixed pixels, sub-pixel fire spot (fire zone) and surrounding background; T_{hi} and T_{bg} are the temperature of sub-pixel fire spots and background; V_i is the central wavenumber of channels; C_1 and C_2 are Planck constants.

For Eq. (4), there are two unknown variables, P and T_{hi}. According to the characteristics of infrared channels in the scanning radiometer (dynamic brightness temperature and spatial resolution), the radiation increase of high-temperature sources varies notably in different bands. To address this issue, a strategy is employed to estimate the actual area and temperature of fire spots according to the radiation in different infrared channels. When the mid-infrared channel was not saturated, it was used for estimating the sub-pixel fire spot area and temperature. Otherwise, the far-infrared channel was alternatively employed for estimation.

When a single channel was adopted to estimate the sub-pixel fire spot area, the fire spot temperature was set to an appropriate value, which was 750 K in this product.

3.3.2 Calculation of fire radiation power

Based on the percentage of sub-pixel fire spot area, P, and fire spot temperature, FRP can be calculated using Stephen–Boltzmann formula:

$$FRP = P * S_{\lambda,\varphi} * \sigma T^4 , \quad (5)$$

where

FRP is fire radiation power, W;

$S_{\lambda,\varphi}$ is the sub-pixel fire spot area of pixels located at longitude λ and latitude φ, which is calculated according to the percentage of sub-pixel fire spot area P and the total pixel area;

T is the sub-pixel fire spot temperature and set to 750 K;

σ is Stephen–Boltzmann constant, 5.6704×10^{-8} (W m^{-2} K^{-4}).

3.4 Verification methods

Wildfires are characterized by random and rapid changes, so it is difficult to verify the product accuracy of GFR (Global Fire) according to actual ground information. In this paper, the accuracy of FY-3 fire products is tested through visual interpretation and cross-verification of other products. Specifically, due to the extreme large size of GFR datasets, we set the different strategies for accuracy assessment. For visual interpretation, several 5-minute data segments with regional representation were selected for verification using manually identified fire spots; For cross-verification with other fire products, global fire spot data throughout 2019 were employed.

The error was defined as the distance from the positions (longitude and latitude) of automatically identified fire spot pixels to corresponding manually identified ones. When the difference in latitude and

https://doi.org/10.5194/essd-2022-27
Preprint. Discussion started: 8 February 2022

longitude was less than or equal to 0.02°, the automatically identified pixel was regarded as a successful identification.

$$\sqrt{(lat1 - lat2)^2 + (long1 - long2)^2} \leq 0.03°$$

where *lat*1 and *lat*2 are the latitude of PGS (Product Generation System) fire spot pixels and manually identified pixels (reference pixels); *long*1 and *long*2 are the longitude of PGS fire spot pixels and manually identified pixels (reference pixels), respectively.

4 Results

4.1 Global-scale test based on visual interpretation

In this research, 5-minute segments of FY-3D fire products in different continents, including Africa, South America, Indo-China Peninsula, Siberia and Australia were collected at 12:15 (UTC) on June 13, 2018, 17: 05 (UTC) on August 21, 2019, 06:15 (UTC) on March 13, 2019, 03:40 (UTC) on November 13, 2019,17:40（UTC）on May 29, 2018 respectively for visual interpretation. The specific observation positions are shown in Fig. 5 with five corresponding fire detection pictures of FY-3D.

These regions were selected for evaluating the global reliability of FY-3D fire products for the following reasons. Firstly, Africa, South America, Indo-China Peninsula, Siberia and Australia are the regions with the most frequent fire events across the globe. Secondly, there are rich vegetation in these regions, which provides the foundation for stable combustion across a year. Thirdly, these regions cover large area with generally unified underlying surfaces. Fourthly, these areas are of regional representation: Siberia represents typical regions with frequent forest fires in Northern Hemisphere. Africa represents typical tropical grasslands and forests in the equator regions. South America represents virgin tropical rainforests.

https://doi.org/10.5194/essd-2022-27
Preprint. Discussion started: 8 February 2022

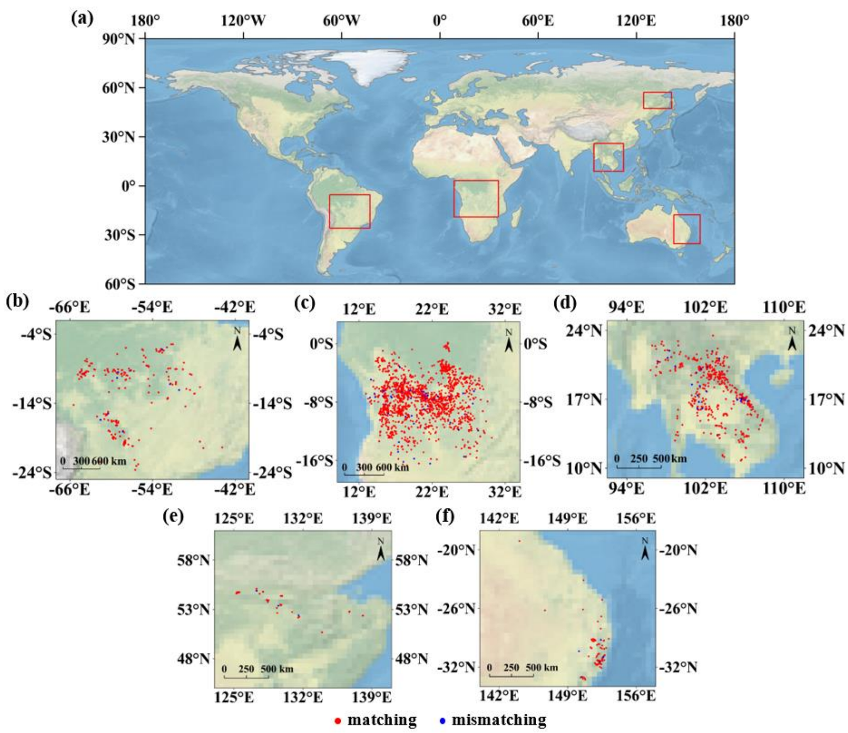

Figure 5 (a), Observation positions from FY-3D MERSI-II. The red frame at the upper right shows FY-3D MERSI-II is located at the border between Northeast China and Russia. The lower left red frame shows FY-3D MERSI-II is over east-central South America and the central red frame shows FY-3D MERSI-II is located in south-central Africa. The middle right red frame shows the FY-3D MERSI-II is over Indo-China Peninsula and the lower right red frame shows the FY-3D MERSI-II is located in east Australia. (b)-(f), Fire spot matching diagram between GFR and visual interpretation data of FY-3D MERSI-II. The red points indicate that GFR matches visual interpretation data, and the blue points represent that only GFR recognized the fire spots, which was not.

Fig. 5 presents the spatial distribution of GFR fire spots and manually identified fire pixels in the 5-minute segment of the above regions. According to Fig 5b, most fire spots in FY-3D products and manually extracted fire spots in South America were in same positions. In Fig 5c, most FY-3D and manually extracted fire spots in Africa coincided or were in a close position. In Fig 5d, despite a few mismatched fire spots, the position of FY-3D and manually extracted fire spots in Indo-China Peninsula was consistent. Fig 5e and Fig 5f also show that most fire spots are matched in Russia and Australia. Table 4 shows accuracy of GFR fire spots in the five typical regions. The accuracy of automatically identified fire spot in all regions was generally consistent and all exceeded 90%. Since these selected regions represented distinct vegetation types and located in different hemispheres, the verification of FY-3D fire products based on 0.24 SMART proved its stability and reliable high-accuracy at the global scale.

Table 4 Verification of fire spot identification based on GFR and SMART in different regions.

https://doi.org/10.5194/essd-2022-27
Preprint. Discussion started: 8 February 2022

Region	GFR-based fire spots	Not match with SMART	Coincidence rate (%)
South-central Africa	1429	77	94.6
East-central South America	204	12	94.1
Siberia	32	3	90.6
Australia	85	7	91.8
Indo-China Peninsula	438	32	92.7
Overall	2188	131	94.0

4.2 Cross-verification with other global fire products

The cross-verification between FY-3D fire products and the mainstream MODIS fire products, MYD14A1 V6 (https://firms.modaps.eosdis.nasa.gov/map/) with a daily temporal resolution and 1km spatial resolution was conducted using the entire 2019 datasets. The data sets with observation time less than 1 h were selected; the underlying surfaces were visually checked to remove areas covered by non-vegetation such as water, ice and snow, and bare land. According to the criterion that the distance matching between the two fire spot pixels was less than 0.03°, cross-verification was conducted with different months, underlying surfaces, regions, and fire intensities. In 2019, there were 2,237,714 fire spot pixels in MODIS fire products, 1,866,920 of which were matched with FY-3D fire products, with an overall consistence of 84.4% (as shown in Fig. 6). As shown in Figure 6, global fire spots were mainly distributed in America, south-central Africa, East, and Southeast Asia, Australia, and parts of Europe, and there were notable spatiotemporal variations of identified fire spots. Specifically, given the overall data volume and spatial distribution, the total number of fire spot pixels from MODIS fire products was larger than FY-3D products. For individual regions, the more fire spots, the higher consistence between FY and MODIS fire products. Africa is the region with the most fire spots across the globe. From May to October, a majority of fire spots was located in southern Africa whilst a majority of fire spots from November to next April was located in the middle and western coastal of Africa. The consistence between MODIS and FY-3D products was higher than other regions. The distribution of fire spots in South America also presented seasonal characteristics. From July to October, fire spots mainly concentrated in middle parts of South America. For other seasons, fire spots in South America mainly concentrated in the North and other parts. The consistence between MODIS and FY-3D fire products also demonstrated seasonal differences, with a high consistence from August to November and a relatively low consistence in other seasons. For Eurasia, there were notable seasonal variations of spatial patterns of fire spots. During March to August, there were relatively many fire spots and the consistence between MODIS and FY-3D fire products was relatively high in this region.

https://doi.org/10.5194/essd-2022-27
Preprint. Discussion started: 8 February 2022

Open Access Earth System Science Data Discussions

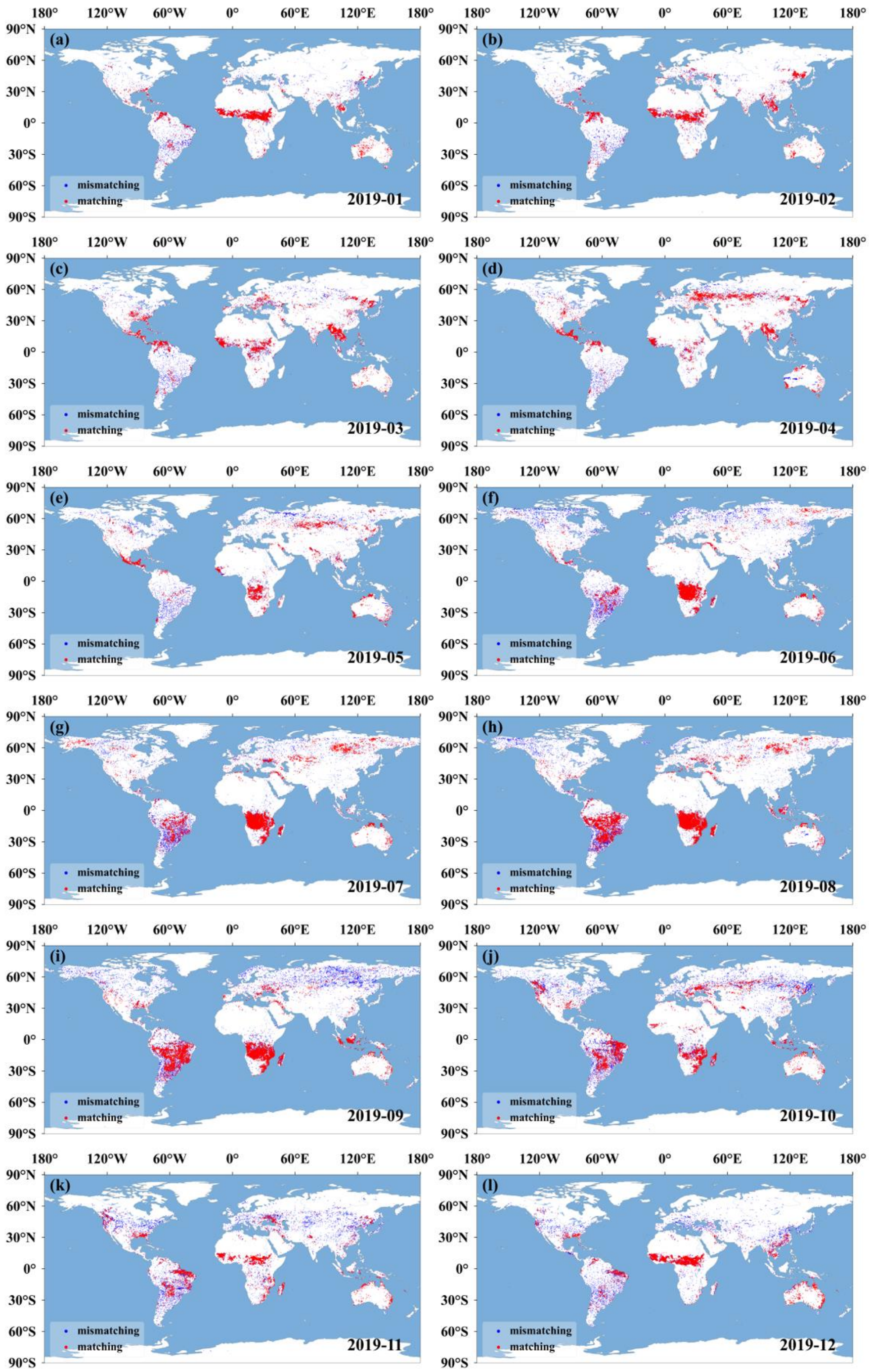

Figure 6 Spatial distribution difference in global fire spots between FY-3D and MODIS fire products in different months of 2019.

https://doi.org/10.5194/essd-2022-27
Preprint. Discussion started: 8 February 2022

In addition to the overall consistence between MODIS and FY-3D fire products, we also conducted cross-verification of the two global fire products in terms of different months, underlying surfaces, regions and fire intensities as follows.

4.2.1 Cross-verification of MODIS and FY-3D in terms of different months

Fig. 7(a) illustrates the monthly precision test of FY-3D and MODIS fire products in 2019. The precision in the remaining months is over 80% except that in April, October, and November. The highest appears in July, exceeding 90%, while the lowest is in April, 71%. Detailed parameters can be found in Table 5. From the global perspective, the number of fire spots was larger in July, August and September and the mean consistence between MODIS and FY-3D fire products was larger than 85%. For July when the fire products were the most, the consistence achieved 90%. From January to May, the number of fire spots was relatively small, and the mean consistence was around 80%. The consistence for April was 71%, lowest among all months. The notable monthly variations of the consistence between MODIS and FY-3D fire products was mainly attributed to the uneven spatial distribution of fire spots across the globe. As shown in Fig 6, in June and July, a large number of fire spots mainly concentrated in Africa, South America and Eurasia, leading to a high consistence of fire identification. In April, there were limited and sparsely distributed fire spots in Africa and South America, leading to a low consistence. According to the statistics, the number of fire spots was positively correlated with the consistence between different fire products. Meanwhile, in seasons when fire could last longer, the consistence was relatively higher.

Table 5 Cross-satellite comparison between FY-3D and MODIS fire products.

Time	Match	Mismatch	Total	Consistence (%)
201901	70799	14188	84987	83
201902	66849	14717	81566	82
201903	105176	22576	127752	82
201904	94474	39250	133724	71
201905	75703	17135	92838	82
201906	174587	33862	208449	84
201907	362108	39683	401791	90
201908	315182	51627	366809	86
201909	226363	47607	273970	83
201910	115975	33956	149931	77
201911	102240	27732	129972	79
201912	157464	28461	185925	85
Total	1866920	370794	2237714	83.4

4.2.2 Cross-verification of MODIS and FY-3D in terms of different underlying surfaces

Statistical analysis of precision is carried out with different types of underlying surfaces. The data of underlying surfaces is the global land use are detailed in Table 6.

https://doi.org/10.5194/essd-2022-27
Preprint. Discussion started: 8 February 2022

The 15 types of underlying surfaces were selected for verification. Table 6 and Fig. 7(c) shows the consistence of FY-3D and MODIS fire products with different underlying surfaces. From the classification of different underlying surfaces, the remaining types are over 80% except (11) Post-flooding or irrigated croplands (or aquatic), (14) Rainfed crops, (20) Mosaic cropland (50-70%) / vegetation (grassland/shrubland/forest) (20-50%), (140) Closed to open (>15%) herbaceous vegetation (grassland, savannas or lichens/mosses), and (150) Sparse (<15%) vegetation. When the underlying surface is the open (15%–40%) coniferous and deciduous forest or evergreen forest, the precision is the highest, at 93%. In addition, according to the classification of underlying surfaces, the fire spot identification shows high precision when the underlying surface is the forest. The consistence between FY-3D and MODIS fire spots on different underlying surfaces in each month was demonstrated in Table 7. Clearly, we can found the fluctuation of consistence across seasons due to the variation of combustible vegetation, which influenced the detecting capability of MODIS and FY-3D.

The low consistence between FY-3D and MODIS fire products was observed for underlying surface 11, 14, 20, 140 and 150. Specifically, 11, 14 and 20 could be categorized as farmlands. 140 was mainly occupied by herbaceous vegetation or sparse grasslands. 150 was mainly occupied by sparse grasslands. Generally, these surfaces were all covered by sparse or unstable vegetation, the fire on which can last for a relatively short period. Meanwhile, the observation time lag between FY-3D and MODIS was larger than 30 minutes. Therefore, the consistence of FY-3D and MODIS fire products on these surface types was lower than other surface types.

Table 6 Classification of underlying surfaces (land cover types).

ID	**Definition of underlying surfaces**
11	Post-flooding or irrigated croplands (or aquatic)
14	Rainfed croplands
20	Mosaic cropland (50-70%) / vegetation (grassland/shrubland/forest) (20-50%)
30	Mosaic vegetation (grassland/shrubland/forest) (50-70%) / cropland (20-50%)
40	Closed to open (>15%) broadleaved evergreen or semi-deciduous forest (>5m)
50	Closed (>40%) broadleaved deciduous forest (>5m)
60	Open (15-40%) broadleaved deciduous forest/woodland (>5m)
70	Closed (>40%) needleleaved evergreen forest (>5m)
90	Open (15-40%) needleleaved deciduous or evergreen forest (>5m)
100	Closed to open (>15%) mixed broadleaved and needleleaved forest (>5m)
110	Mosaic forest or shrubland (50-70%) / grassland (20-50%)
120	Mosaic grassland (50-70%) / forest or shrubland (20-50%)
130	Closed to open (>15%) (broadleaved or needleleaved, evergreen or deciduous) shrubland (<5m)
140	Closed to open (>15%) herbaceous vegetation (grassland, savannas or lichens/mosses)
150	Sparse (<15%) vegetation

https://doi.org/10.5194/essd-2022-27
Preprint. Discussion started: 8 February 2022

Table 7 the consistence between FY-3D and MODIS fire spots on different underlying surfaces in each month (total FY-3D pixels (matched percentage)).

ID	Jan	Feb	Mar	Apr	May	Jun	Jul	Aug	Sep	Oct	Nov	Dec
11	754 (50%)	1471(76%)	1651(86%)	450(81%)	201(68%)	344(66%)	353(54%)	678(77%)	1786(80%)	1516(85%)	558(73%)	416(56%)
14	4459(64%)	5024(57%)	7745(73%)	11439(81%)	6818(71%)	4137(64%)	2135(56%)	4122(79%)	8090(85%)	4561(73%)	3154(73%)	1663(57%)
20	8033(72%)	8596(67%)	13513(78%)	20282(83%)	14772(78%)	5216(68%)	2921(64%)	5449(81%)	11970(87%)	5858(73%)	4721(77%)	5572(79%)
30	5786(65%)	7227(63%)	13018(77%)	22626(84%)	26523(82%)	23024(84%)	16007(84%)	6455(77%)	14534(83%)	16523(83%)	8646(79%)	5199(75%)
40	45313(94%)	38194(88%)	25315(75%)	63474(84%)	69987(85%)	14770(74%)	8265(72%)	7107(76%)	22921(83%)	31839(83%)	14646(80%)	9556(82%)
50	3454(61%)	8398(72%)	19960(82%)	45387(88%)	51148(87%)	42981(86%)	25424(85%)	4356(71%)	5481(81%)	6237(79%)	3713(80%)	1920(66%)
60	36987(90%)	6321(85%)	5570(75%)	25021(87%)	49083(86%)	74660(89%)	59345(89%)	6526(82%)	3028(82%)	4478(79%)	12513(86%)	18192(89%)
70	1863(56%)	3655(79%)	5031(80%)	4052(87%)	1865(82%)	3411(90%)	2123(73%)	3402(86%)	2346(82%)	2791(77%)	704(49%)	719(66%)
90	840(35%)	3255(57%)	8901(62%)	11125(56%)	61299(97%)	135344(98%)	32767(91%)	18539(85%)	4645(64%)	4076(72%)	1484(82%)	608(56%)
100	1079(49%)	1851(59%)	3423(71%)	1988(59%)	2444(82%)	6027(93%)	3677(87%)	8695(92%)	2813(70%)	2596(75%)	565(70%)	397(66%)
110	19896(84%)	13825(84%)	4194(73%)	3669(67%)	6504(80%)	11351(92%)	7407(84%)	7223(88%)	4268(84%)	4983(86%)	5009(86%)	5409(81%)
120	6568(83%)	3406(81%)	3639(77%)	3602(65%)	9037(86%)	12972(93%)	7122(86%)	4999(85%)	3574(51%)	2379(84%)	4651(88%)	4710(87%)
130	38258(87%)	18784(85%)	19935(85%)	34627(87%)	37668(84%)	34189(86%)	20881(85%)	6963(76%)	20071(85%)	27134(87%)	8320(82%)	15465(84%)
140	3941(76%)	2905(66%)	6159(78%)	7692(80%)	6756(76%)	8964(85%)	5139(78%)	3104(80%)	13060(26%)	3562(82%)	3844(87%)	4270(87%)
150	5760(77%)	5073(71%)	8872(77%)	7268(60%)	15938(81%)	19370(87%)	10467(58%)	4106(71%)	12991(24%)	3532(75%)	6359(88%)	8994(92%)

https://doi.org/10.5194/essd-2022-27
Preprint. Discussion started: 8 February 2022

4.2.3 Cross-verification of MODIS and FY-3D in terms of different regions

The global monitoring area is divided into Africa, America, Asia, Europe, and Oceania. The verification demonstrates the results with the highest precision (over 80%) are found in Africa and Asia, and those in America, Europe, and Oceania show the precision over 70%. The FY-3D/MERSI-II fire identification algorithm draws lessons from the MODIS algorithm and has been improved on that basis, and targeted development has been made for the underlying surface and climatic conditions in China, so it is necessary to test the matching results in China separately. It shows that China's regional consistency of results in China is lower than other continents, only 65%. Compared with other continents, the low consistence between FY-3D and MODIS fire products in China may be attributed to the following reason. Thanks to the field-collected data, the algorithm for fire detection using FY-3D specifically included the underlying surfaces and surrounding geographical conditions in China. Therefore, FY-3D has the potential to provide more reliable fire products for China.

According to the feedback on practical application in China, especially during the period from July to September, when there were much precipitation, cloud cover, there should be limited fire spots identified. However, based on MODIS fire products, there were many fire spots during this period, which were much more than FY-3D detected fire spots. The consistence between MODIS and FY-3D fire products in China was only 65%. Specifically, the fire spot precision of FY-3D/MERI-II was higher than 85%, which indicated that the precision of the MODIS algorithm is inferior to FY-3D/MERI-II in China with the decline in instrument performance (see Fig. 7(b) for details).

https://doi.org/10.5194/essd-2022-27
Preprint. Discussion started: 8 February 2022

Open Access Earth System Science Data Discussions

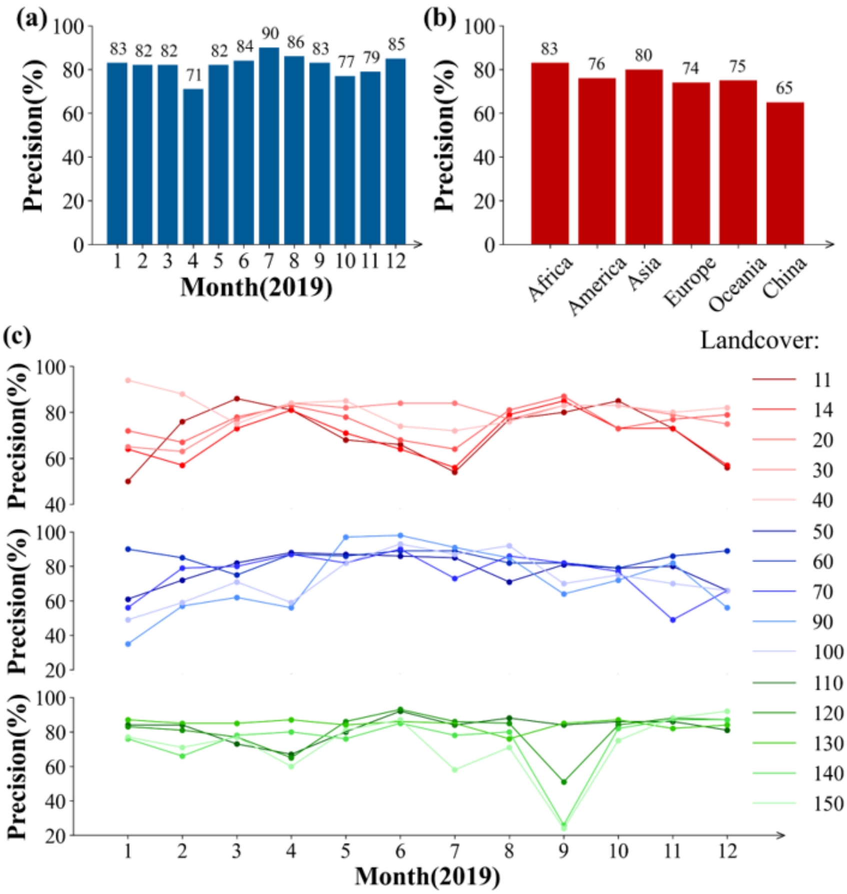

Figure 7 (a)-(c). (a): Monthly precision test of fire spots identified by FY-3d and MODIS fire products. (b): Precision test of fire spots identified by FY-3D and MODIS fire products in different regions. (c): Monthly precision test of fire spots identified by FY-3d and MODIS fire products with different underlying surfaces.

4.2.4 Cross-verification of MODIS and FY-3D in terms of fire intensities

The confidence of fire spots and the fire intensity represented by FRP are analyzed respectively, and the data comes from the MODIS fire spot list. Fig. 8(a) and Fig. 8(b) are statistical diagrams of confidence and FRP, respectively. From Fig. 8(a), the confidence of the matched pixels of the two satellites is above 66%, while that of the mismatched ones is less than 60% and even lower than 50% in some months. In other words, the higher confidence indicates the higher matching degree. As indicated by Fig. 8(b), the FRP of the matched pixels of two satellites is mostly above 40 MW, while that of the unmatched pixels is less than 40 MW and even lower than 20 MW in some months. Accordingly, the greater fire intensity leads to the greater probability of simultaneous observation by the two satellites and the higher matching degree between their results.

https://doi.org/10.5194/essd-2022-27
Preprint. Discussion started: 8 February 2022

Two major findings were identified based on the comparison between FY-3D and MODIS fire products in terms of fire intensity: Firstly, the higher the credential of the identified fire, the higher consistence between FY-3D and MODIS fire products. When the credential was larger than 65%, both FY-3D and MODIS could effectively identify the candidate pixel as fire pixel. In other words, the parameter of credential in MODIS fire product provides important reference for fire detection. Secondly, FRP is an index for the heat radiation of the fire. The larger FRP, the larger consistence between FY-3D and MODIS was, indicating a higher accuracy of fire detection. Therefore, the difficulty for fire detection mainly lies in the detection of weak fires.

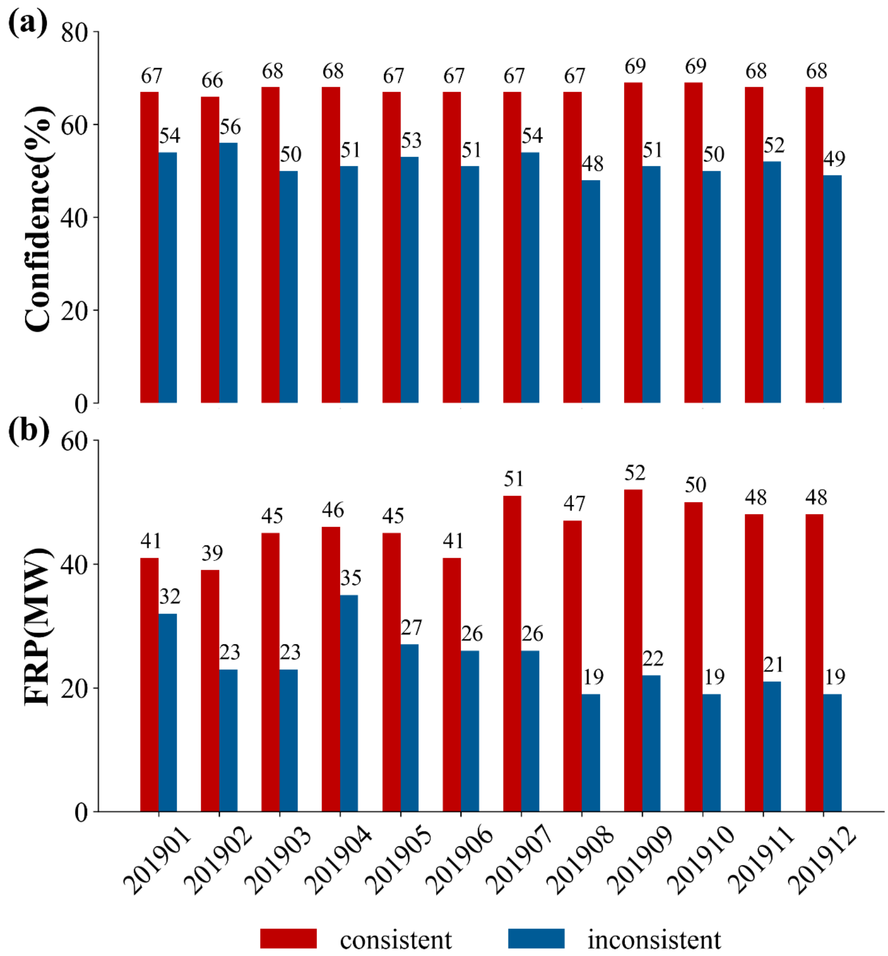

Figure 8 (a)-(b). (a):Relationship between matching and confidence of different fire spots. (b): Relationship between matching and FRP of different fire spots.

https://doi.org/10.5194/essd-2022-27
Preprint. Discussion started: 8 February 2022

5 Discussion

5.1 Advantages, limitations and implementations of FY-3D fire products

As satellite instruments keep aging in the harsh space environment, the degradation of sensors is inevitable. Theoretically, sensor degradation can be corrected through atmospheric calibration. However, during the mission life, the solar diffuser and stability monitor required for atmospheric calibration also change across time (Wang et al., 2012). Since the MODIS instrument has been working for nearly 20 years, its performance for fire detection degrades notably. Furthermore, similar to VIIRS and other algorithms, MODIS fire products may have large uncertainties in such regions as China (Fu et al., 2020; Ying et al., 2019).

As one major product of the FY-3D meteorological satellite, FY-3D fire product boasts the highest resolution and precision in China by specifically including the underlying surface parameters collected in China. Compared with MODIS and VIIRS, MERSI-II shows the resolution of 250 m in the far-infrared channel, which is the highest among meteorological satellites of the same type. The FY-3D fire identification algorithm learns from the advantages and technical ideas of MODIS and VIIRS fire-identification algorithms. Furthermore, FY-3D fire products have been optimized in terms of auxiliary parameters, fire identification, and re-identification as follows:

Auxiliary parameters：Since the sole use of vegetation index is limited to reflect combustible materials, climatic boundaries and geographical environment data, which had a strong influence on vegetation types and growth, were added to FY-3D fire identification.

Fire identification: FY-3D adopts the adaptive threshold and reduces the limitations caused by fixed thresholds of MODIS and VIIRS algorithms. Meanwhile, FY employs a re-identification index according to geographical latitude, underlying surface types, as well as the influence by cloud, water bodies and bare land and the comprehensive consideration of multiple influencing factors increases the accuracy of fire identification; Thirdly, since the far-infrared channel plays an important role in fire identification and FY-3D has a high resolution of 250 m in the far-infrared channel, The precision of fire identification is improved.

Fire re-identification: FY-3D fire products can be used for both global climate change research and such practical implementations as forest and grassland fire prevention with a higher requirement for precision. Based on the initially identified fire spots, FY-3D employed the re-identification index to further remove fire spots at cloud edges, cloud gaps, water body edges, and conventional heat sources and on bare land and highly reflective underlying surfaces.

MODIS fire product is one of the most significant and frequently employed fire products with mature algorithms. Compared with MODIS, FY-3D receives limited emphasis for its capability of fire monitoring, which is mainly attributed to its short service periods. On one hand, due to its long time series and general reliability, MODIS fire products remained a major choice for monitoring long-term variations of fire spots across the world. However, the continuous degradation of MODIS sensors led to large uncertainties to the quality of recent and future MODIS fire products. In this case, thanks to its

https://doi.org/10.5194/essd-2022-27
Preprint. Discussion started: 8 February 2022

similar spatio-temporal resolution and high precision, FY-3D fire product has the potential to be widely employed as the replacement and continuity of global MODIS fire products. Meanwhile, FY-3D fire products have a higher reliability in China and its surrounding regions than other fire products. Therefore, FY-3D fire products are an ideal selection for fire monitoring across China.

The main implementation of FY-3D fire products is fire monitoring. For vast forest and grassland areas, it is inefficient and time-consuming for manual and aircraft patrol to monitor wildfires. Satellite remote sensing can work for continuous space with a wide monitoring range, providing massive information in fire detection, disaster relief, and post-disaster assessment.

In addition to the fire spot identification and real-time fire tracking, the impact of pollutants produced by biomass combustion on the environment is another important topic. In China and Southeast Asia, air pollution caused by biomass burning has been intensified in recent years. Agricultural activities such as crop-residue burning and wildfires (e.g. forest fires and grassland fires) emit airborne pollutants (e.g. $PM_{2.5}$, PM_{10}, CO). In this regard, FY-3D fire products can be used as the emission sources for estimating its environmental effects.

5.2 Future extension of FY-3D fire products

China has just launched FY-3E and FY-4B satellites in June and July, 2021. Amid the launch and operation of a new generation of Fengyun meteorological satellites, the accuracy and timeliness of fire monitoring by meteorological satellites have been largely enhanced. Thanks to the improved meteorological data, which provides useful reference to understand the current status of combustibles and potential fire risk, FY-3D satellite will be taken as a better data source to produce various secondary products for fire monitoring and prediction. Based on traditional fire spot identification, further research should concentrate on the assessment of fire area, estimation of biomass carbon emission, prediction of smoke impact, and early warning of forest and grassland fire using the series of Fengyun meteorological satellites. For instance, the water content of combustibles is closely related to temperature, light, and cloud cover, which is an important indicator in forest and grassland fire forecasts. However, this variable was rarely considered in previous fire products. Based on the series of products of Fengyun meteorological satellites such as surface temperature, vegetation index, surface evapotranspiration, solar radiance, and cloud cover, FY-3D fire products can be improved by establishing an estimation model for the water content of combustibles. Meanwhile, with the fire products such as fire spot and smoke, and the meteorological products such as wind field data from Fengyun series satellites, we can predict the impact of smoke caused by forest and grassland fires on the atmospheric environment in the surrounding and even remote areas. In the future implementations, Fengyun meteorological satellites will play a greater role in monitoring, early warning, and forecast of global fires and their ecological impacts.

6 Data availability

The MYD14A1 Version 6 is available via the NASA FIRMS portal (https://firms.modaps.eosdis.nasa.gov/map/, NASA FIRMS, 2021). FY-3D fire products are now downloadable from our official website (http://satellite.nsmc.org.cn/portalsite/default.aspx, NSMC, 2021) using registered account and password. For the convenience of data check and trial experiments, a test account is provided as

Account: 1256931756@qq.com

Password: yangjing1211

7 Conclusions

With a similar spatial and temporal resolution, we produced FY-3D global fire products, aiming to serve as the continuity and replacement for MODIS fire products, which has been degrading after long-term service. The sensor parameters and major algorithms for noise detection and fire identification in FY-3D products were introduced. For accuracy assessment, five typical regions, Africa, South America, Indo-China Peninsula， Siberia and Australia, across the globe were selected and the overall consistence between FY-3D fire products and reference data exceeded 94%, with a more than 90% consistence in all regions. We also compared the FY-3D and MODIS fire products for their consistence. The result suggested that the overall consistence was 84.4%, with a fluctuation across seasons, surface types and regions. The high accuracy and consistence with MODIS products proved that FY-3D fire product was an ideal tool for global fire monitoring. Specially, since detailed geographical conditions in China were considered, FY-3D products should be preferably employed for monitoring fires and estimating its environment effects in China.

Author contributions

J, C., W.Z and C,L produced FY-3D global fire products and the official website. J.C., Z.C., B, G., M, L. conceived the manuscript. J,C., C,Z., Q, Y., M.X., X,C., and J, Y. conducted data analysis and produced Figures. J.C and Z.C wrote the draft. Z.C and M,L. reviewed and revised the manuscript.

Competing interests

The authors have no competing interests.

Financial support

This work was supported by the National Natural Science Foundation of China (Grant No.42171399) and National Key R&D Program of China (2021YFC3000300).

https://doi.org/10.5194/essd-2022-27
Preprint. Discussion started: 8 February 2022

References

Abram, N.J., Henley, B.J. and Sen Gupta, A.: Connections of climate change and variability to large and extreme forest fires in southeast Australia, Commun. Earth Environ., 2, 8, https://doi.org/10.1038/s43247-020-00065-8, 2021.

Alisjahbana, A.S. and Busch, J.M.: Forestry, Forest Fires, and Climate Change in Indonesia. Bull. of Indones. Econ. Stud., 53, 111–136, https://doi.org/10.1080/00074918.2017.1365404, 2017.

Andela, N., Morton, D.C., Giglio, L., Paugam, R., Chen, Y., Hantson, S., van der Werf, G. R., and Randerson, J.T.: The Global Fire Atlas of individual fire size, duration, speed and direction, Earth Syst. Sci. Data, 11, 529–552, https://doi.org/10.5194/essd-11-529-2019, 2019.

Boles, S.H. and Verbyla, D.L.: Comparison of three AVHRR-based fire detection algorithms for interior Alaska, Remote Sens. Environ., 72, 1-16, https://doi.org/10.1016/S0034-4257(99)00079-6, 2000.

Cerda, Lloret, F., Ruiz, J.E., and Vandermeer, J.H.: Tree mortality following ENSO-associated fires and drought in lowland rain forests of Eastern Nicaragua, For. Ecol. Manage., 265, 248-257, https://doi.org/10.1016/j.foreco.2011.10.034, 2012.

Cochrane, M.: Fire science for rainforests, Nature, 421, 913-919, https://doi.org/10.1038/nature01437, 2003.

Dozier, J.: A method for satellite identification of surface temperature fields of subpixel resolution, Remote Sens. Environ., 74, 33-38, https://doi.org/10.1016/0034-4257(81)90021-3, 1981.

Flannigan, M.D. and Haar, T.H.: Forest fire monitoring using NOAA satellite AVHRR, Can. J. For. Res., 16, 975-982, https://doi.org/10.1139/x86-171, 1986.

Giglio, L., Descloitres, J., Justice, C.O., and Kaufman, Y.J.: An Enhanced Contextual Fire Detection Algorithm for MODIS, Remote Sens. Environ., 87, 273-282, https://doi.org/10.1016/S0034-4257(03)00184-6, 2003.

Guo, L., Ma, Y., Tigabu, M., Guo, X., Zheng, W., and Guo, F.: Emission of atmospheric pollutants during forest fire in boreal region of China, Environ. Pollut., 264, 114709, https://doi.org/10.1016/j.envpol.2020.114709, 2020.

Huff, A.K., Kondragunta, S., Zhang, H., and Hoff, R.M.: Monitoring the impacts of wildfires on forest ecosystems and public health in the exo-urban environment using high-resolution satellite aerosol products from the visible infrared imaging radio-meter suite (VIIRS), Environ. Health Insights, 9s2, EHI.S19590, https://doi.org/10.4137/ehi.s19590, 2015.

Jacobson, M.Z.: Effects of biomass burning on climate, accounting for heat and moisture fluxes, black and brown carbon, and cloud absorption effects, J. Geophys. Res. Atmos., 119, 2014JD021861, https://doi.org/10.1002/2014JD021861, 2014.

Jethva, H., Torres, O., and Field, R.D.: Connecting Crop Productivity, Residue Fires, and Air Quality over Northern India, Sci. Rep., 9, 16594, https://doi.org/10.1038/s41598-019-52799-x, 2019.

Johnston, F.H., Henderson, S.B., Chen, Y., Randerson, J.T., Marlier, M., DeFries, R.S., Kinney, P., Bowman, D.M., and Brauer, M.: Estimated global mortality attributable to smoke from landscape fires, Environ. Health Perspect, 120, https://doi.org/10.1289/ehp.1104422, 2012.

Kaufman, Y.J., Setzer, A., and Justice, C.: Remote Sensing of Biomass Burning in the Tropics,

https://doi.org/10.5194/essd-2022-27
Preprint. Discussion started: 8 February 2022

Fire in the Tropical Biota, 84, 371-399, https://doi.org/10.1007/978-3-642-75395-4_16, 1990.

Keegan, K.M., Albert, M.R., McConnell, J.R., and Baker, I.: Climate change and forest fires synergistically drive widespread melt events of the Greenland Ice Sheet, Proc. Natl. Acad. Sci. U.S.A., 111, 7964–7967, https://doi.org/10.1073/pnas.1405397111, 2014.

Keeley, J.E., Bond, W.J., Bradstock, R.A., Pausas, J.G., and Rundel, P.W.: Fire in Mediterranean ecosystems: Ecology, evolution and management, Cambridge University Press, Cambridge, United Kingdom, 2011.

Kelly, L.T., Giljohann, K.M., Duane, A., Aquilué, N., Archibald, S., and Batllori, E.: Fire and biodiversity in the Anthropocene, Science, 370, eabb0355, https://doi.org/10.1126/science.abb0355, 2020.

Kumar, S.S. and Roy, D.P.: Global operational land imager Landsat-8 reflectance-based active fire detection algorithm, Int. J. Digit. Earth, 11, 154-178, https://doi.org/10.1080/17538947.2017.1391341, 2017.

Li, F., Zhang, X., Kondragunta, S., and Lu, X.: An evaluation of advanced baseline imager fire radiative power based wildfire emissions using carbon monoxide observed by the Tropospheric Monitoring Instrument across the conterminous United States, Environ. Res. Lett., 15, 094049, https://doi.org/10.1088/1748-9326/ab9d3a, 2020.

Li, J., Bo, Y., and Xie, S.: Estimating emissions from crop residue open burning in China based on statistics and MODIS fire products, J. Environ. Sci., 44, 158-170, https://doi.org/10.1016/j.jes.2015.08.024, 2016.

Lin, Z., Chen, F., Li, B., Yu, B., Shirazi, Z., Wu, Q., and Wu, W.: FengYun-3C VIRR Active Fire Monitoring: Algorithm Description and Initial Assessment Using MODIS and Landsat Data, IEEE Trans. Geosci. Remote Sens., 55, 6420-6430, https://doi.org/10.1109/TGRS.2017.2728103, 2017.

Liu, T., Marlier, M.E., DeFries, R.S., Westervelt, D.M., Xia, K.R., Fiore, A.M., Mickley, L.J., Cusworth, D.H., and Milly, G.: Seasonal impact of regional outdoor biomass burning on air pollution in three Indian cities: Delhi, Bengaluru, and Pune, Atmos. Environ, 172, 83–92, https://doi.org/10.1016/j.atmosenv.2017.10.024, 2018.

Marlier, M.E., DeFries, R.S., Kim, P.S., Koplitz, S.N., Jacob, D.J., Mickley, L.J., and Myers, S.S.: Fire emissions and regional air quality impacts from fires in oil palm, timber, and logging concessions in Indonesia, Environ. Res. Lett, 10, 085005, https://doi.org/10.1088/1748-9326/10/8/085005, 2015.

Matson, M. and Schneider, S.R.: Fire Detection Using the NOAA-Series Satellite, NOAA Technical Report NESDIS, 7, 1984.

Mohajane, M., Costache, R., Karimi, F., Pham, Q.B., Essahlaoui, A., Nguyen, H., Laneve, G., and Oudija, F.: Application of remote sensing and machine learning algorithms for forest fire mapping in a Mediterranean area, Ecol. Indic., 129, 107869, https://doi.org/10.1016/j.ecolind.2021.107869, 2021.

Moritz, M.A., Parisien, M.A., Batllori, E., Krawchuk, M.A., Van Dorn, J., Ganz, D.J., and Hayhoe, K.: Climate change and disruptions to global fire activity, Ecosphere, 3, 1–22, https://doi.or

https://doi.org/10.5194/essd-2022-27
Preprint. Discussion started: 8 February 2022

Open Access Earth System Science Data Discussions

g/10.1890/ES11-00345.1, 2012.

Murphy, S.W., Filho, C.R., Wright, R., Sabatino, G., and Pabon, R.C.: HOTMAP: Global hot target detection at moderate spatial resolution, Remote Sens. Environ., 177, 78-88, https://doi.org/10.1016/j.rse.2016.02.027, 2016.

NASA FIRMS: MODIS fire products MYD14A1 V6.1 2019 [data set], available at: https://firms.modaps.eosdis.nasa.gov/map/, last access 10 January 2021.

NSMC: FY-3D fire products 2018-2019 [data set], available at: http://satellite.nsmc.org.cn/portalsite/default.aspx, last access 10 January 2021.

Oliveira, M., Delerue-Matos, C., Pereira, M.C., and Morais, S.: Environmental Particulate Matter Levels during 2017 Large Forest Fires and Megafires in the Center Region of Portugal: A Public Health Concern? Int. J. Environ. Res. Public Health, 17, 1032, https://doi.org/10.3390/ijerph17031032, 2020.

Schroeder, W., Oliva, P., and Giglio, L.: The New VIIRS 375 m active fire detection data product: Algorithm description and initial assessment, Remote Sens. Environ., 143, 85-96, https://doi.org/10.1016/j.rse.2013.12.008, 2014.

Kaufman, Y.J., Kleidman, R.G., and King, M.D.: SCAR-B fires in the tropics: properties and remote sensing from EOS-MODIS, J. Geophys. Res. Atmos., 103(D24): 31955-31968, https://doi.org/10.1029/98JD02460, 1998.

Schroeder, W., Oliva, P., Giglio, L., Quayle, B., Lorenz, E., and Morelli, F.: Active fire detection using Landsat-8/OLI data, Remote Sens. Environ., 185, 210-220, https://doi.org/10.1016/j.rse.2015.08.032, 2016.

Sharma, A., Wang, J., and Lennartson, E.M.: Intercomparison of MODIS and VIIRS Fire Products in Khanty-Mansiysk Russia: Implications for Characterizing Gas Flaring from Space, Atmosphere, 8, 95, https://doi.org/10.3390/atmos8060095, 2017.

Stephenson, C., Handmer, J., and Betts, R.: Estimating the economic, social and environmental impacts of wildfires in Australia, Environ. Hazards, 12, 93–111, https://doi.org/10.1080/17477891.2012.703490, 2013.

Volkova, L., Roxburgh, S.H., Surawski, N.C., Meyer, C.P., and Weston, C.J.: Improving reporting of national greenhouse gas emissions from forest fires for emission reduction benefits: An example from Australia, Environ. Sci. Policy, 94, 49-62. https://doi.org/10.1016/j.envsci.2018.12.023, 2019.

Wang, D., Morton, D., Masek, J., Wu, A., Nagol, J., Xiong, X., Levy, R., Vermote, E., and Wolfe, R.: Impact of sensor degradation on the MODIS NDVI time series, Remote Sens. Environ., 119, 55-61, https://doi.org/10.1016/j.rse.2011.12.001, 2012.

Wickramasinghe, C., Wallace, L., Reinke, K., and Jones, S.: Intercomparison of Himawari-8 AHI-FSA with MODIS and VIIRS active fire products, Int. J. Digit. Earth, 13, 457-473, https://doi.org/10.1080/17538947.2018.1527402, 2018.

Wintle, B.A., Legge, S., and Woinarski, J.: After the Megafires: What Next for Australian Wildlife? Trends Ecol. Evol., 35, 753-757, https://doi.org/10.1016/j.tree.2020.06.009, 2020.

https://doi.org/10.5194/essd-2022-27
Preprint. Discussion started: 8 February 2022

Xu, W., Wooster, M.J., Kaneko, T., He, J., Zhang, T., and Fisher, D.: Major advances in geostationary fire radiative power (FRP) retrieval over Asia and Australia stemming from use of Himarawi-8 AHI, Remote Sens. Environ., 193, 138-149, https://doi.org/10.1016/j.rse.2017.02.024, 2017.

Yuchi, W., Yao, J., Kathleen, E.M., Roland, S., Radenko, P., Didier, D., Michael, D.M., and Sarah, B.H.: Blending forest fire smoke forecasts with observed data can improve their utility for public health applications, Atmos. Environ., 145, 308-317, https://doi.org/10.1016/j.atmosenv.2016.09.049, 2016.

Zhang, Z., Feng, Z., Zhang, H., Zhao, J., Yu, S., and Du, W.: Spatial distribution of grassland fires at the regional scale based on the MODIS active fire products. Int. J. Wildland Fire, 26, 209-218, https://doi.org/10.1071/WF16026, 2017.